THE JOURNAL OF PHYSICAL CHEMISTRY A

Article

Cite This: J. Phys. Chem. A 2019, 123, 7897−7910

pubs.acs.org/JPCA

Oxidation Kinetics and Thermodynamics of Resonance-Stabilized Radicals: The Pent-1-en-3-yl + O_2 Reaction

Malte Döntgen,[†,‡] Timo T. Pekkanen,[†] Satya P. Joshi,[†] Raimo S. Timonen,[†] and Arkke J. Eskola*[,†]

[†]Department of Chemistry, University of Helsinki, P.O. Box 55 (A.I. Virtasen aukio 1), FI-00014, Helsinki, Finland

[‡]School of Engineering, Brown University, Providence, Rhode Island 02912, United States

Supporting Information

ABSTRACT: The kinetics and thermochemistry of the pent-1-en-3-yl radical reaction with molecular oxygen ($CH_2CHCHCH_2CH_3$ + O_2) has been studied by both experimental and computational methods. The bimolecular rate coefficient of the reaction was measured as a function of temperature (198−370 K) and pressure (0.2−4.5 Torr) using laser photolysis−photoionization mass-spectrometry. Quantum chemical calculations were used to explore the potential energy surface of the reaction, after which Rice−Ramsperger−Kassel−Marcus theory/master equation simulations were performed to investigate the reaction. The experimental data were used to adjust key parameters, such as well depths, in the master equation model within methodological uncertainties. The master equation simulations suggest that the formation rates of the two potential RO_2 adducts are equal and that the reaction to QOOH is slower than for saturated hydrocarbons. The initial addition reaction, $CH_2CHCHCH_2CH_3$ + O_2, is found to be barrierless when accounting for multireference effects. This is in agreement with the current experimental data, as well as with past experimental data for the allyl + O_2 reaction. Finally, we conducted numerical simulations of the pent-1-en-3-yl + O_2 reaction system and observed significant amounts of penta-1,3-diene being formed under engine-relevant conditions.

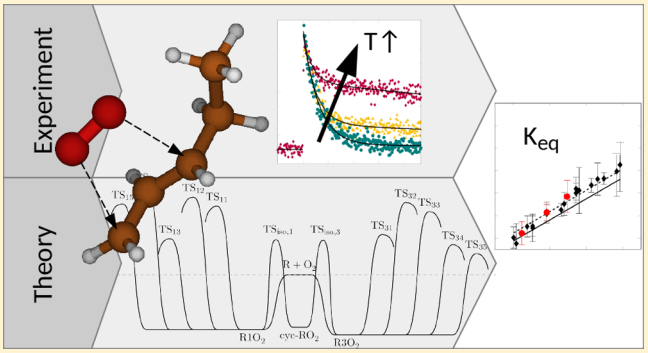

INTRODUCTION

Both conventional fuels[1] and biofuels[2,3] contain unsaturated hydrocarbons, which are known to form resonance-stabilized radicals when hydrogen atoms are abstracted from their allylic site(s).[4,5] Unsaturated hydrocarbons are also produced in the combustion of saturated hydrocarbons (R + O_2 → alkene + HO_2). The oxidation kinetics and thermochemistry of resonance-stabilized radicals are key in the detailed kinetic modeling of, for example, plant oil-derived biodiesel,[2] and differ significantly from hydrocarbon radicals that are not resonance stabilized.[6,7] Consequently, analogies to saturated hydrocarbon radicals are questionable and detailed studies on oxidation kinetics and thermochemistry of resonance-stabilized radicals are needed. In this work, the pent-1-en-3-yl + O_2 reaction is studied by both experimental and computational methods and the results are compared with previous studies on smaller allyl-type radicals.

The smallest resonance-stabilized hydrocarbon radicals, allyl (C_3H_5) and propargyl (C_3H_3), are the most extensively studied resonance-stabilized radicals.[6−14] The reaction of allyl + O_2 was first assumed to be barrierless,[9] but later revisions by Lee and Bozzelli[7] showed that the reaction has a barrier of about 1 kcal/mol at the CBS-Q level of theory. Moreover, the allylperoxy radical was found to be thermochemically less stable compared to the propylperoxy radical (well depths of 19[7] and 34 kcal/mol,[15] respectively). Chen and Bozzelli[16] showed that substituting a hydrogen atom at the secondary carbon of the allyl radical with a methyl group has an insignificant effect on the RO_2 well depth and barrier, which amount to 20 and 1.5 kcal/mol for the allylic isobutenyl radical at the QCISD(T)//B3LYP level of theory, respectively. For longer linear resonance-stabilized radicals, the oxidation chemistry has been addressed via kinetic modeling,[17,18] but elementary oxidation reactions were not studied in detail. Experimental studies on the kinetics of allyl-type radicals with molecular oxygen are scarce.[12,19] Potentially the most definitive study elucidating the reaction of resonance-stabilized radicals with O_2 is the work of Moradi et al.[13] on propargyl + O_2. The authors combined liquid helium droplet experiments with high-level quantum chemical calculations and consistently found that the O_2 addition to the propargyl radical is a barrierless reaction. It is unclear, however, if the findings for the propargyl radical + O_2 reaction can be extrapolated to allyl-type radicals.

Except for the work of Moradi et al.,[13] the above-discussed literature on linear and branched resonance-stabilized radicals employed ab initio methods based on single-reference wave functions. For radical−radical recombination reactions, how-

Received: April 26, 2019
Revised: August 14, 2019
Published: August 26, 2019

DOI: 10.1021/acs.jpca.9b03923
J. Phys. Chem. A 2019, 123, 7897−7910

ever, Harding et al.[20] stated that single-reference association potentials (interaction energy along the minimum energy path) increasingly deviate from the full configuration interaction association potentials with increasing radical−radical distance and that multireference wave functions have to be used. Furthermore, if a resonance-stabilized radical was involved in the reaction, the active space for multireference calculations required for accurately describing the reaction kinetics needs to include the electrons and orbitals involved in resonance stabilization.[13] In allylic hydrocarbon radicals, the active space comprises one orbital for each pair of the neighboring atoms involved in the stabilized system and one orbital for the two possible association sites. When forming a chemical bond with either the association site, the pair-wise orbital not involving the association site will give a double bond, while the radical orbital will change in favor of the association site.

In this study, the initial association potential of pent-1-en-3-yl + O_2 has been calculated both by single and multireference methods to investigate the possible presence of a reaction barrier in the allylic system. The experimental and theoretical results will be combined synergistically to provide reliable kinetics and thermochemistry. These results will be compared with the allyl + O_2 and isobutenyl + O_2 reactions to investigate how the molecular structure affects the reactivity of allyl-type radicals with molecular oxygen. Finally, the pent-1-en-3-yl + O_2 oxidation reaction is simulated under low temperature combustion conditions using the kinetic parameters obtained in this work.

EXPERIMENTAL METHODS

An extensive description of the experimental apparatus and data analysis procedure is given in a publication by Eskola and Timonen,[21] so only a short summary of the relevant experimental details is given here. The experiments were performed at low pressures (0.18−4.5 Torr) in a temperature-controlled laminar flow reactor coupled to a photoionization mass spectrometer. Stainless steel (d = 0.80 or 1.7 cm, halocarbon wax coating) and quartz (d = 0.85 or 1.7 cm, boric oxide coating) reactors were used in the experiments.

The radical precursor (*trans*-1-bromopent-2-ene, purity > 95% or *trans*-1-chloropent-2-ene, purity > 95%) was introduced into a reactor by bubbling helium through a liquid precursor that had been degassed by several freeze−pump−thaw cycles. The vapor pressures of the precursors were used to estimate the concentration of the precursor in the reactor.[22] Helium (purity 99.9996%) and oxygen (purity 99.9995%) were used as supplied. The radicals were homogeneously produced along the reactor by photolyzing the precursor molecules with pulsed KrF exciplex laser radiation (248 nm). The laser fluence used was 15−140 mJ·cm^{-2}. The main photolysis reaction of the precursors at 248 nm is the dissociation of the C−Br/C−Cl bond at the allylic site

$$CH_2Br{-}CH{=}CH{-}CH_2{-}CH_3 \longrightarrow CH_2{=}CH{=}CH{-}CH_2{-}CH_3 + Br \quad (1)$$

$$CH_2Cl{-}CH{=}CH{-}CH_2{-}CH_3 \longrightarrow CH_2{=}CH{=}CH{-}CH_2{-}CH_3 + Cl \quad (2)$$

The measurements were performed under pseudo-first-order conditions ($[O_2] \gg [C_5H_9]$) and the initial radical concentration ($[R]_{t=0}$) was kept low to avoid complications from the self-reaction of the radical. The radical concentration was estimated to be smaller than 3 × 10^{11} cm^{-3} in all measurements. The gas mixture was continuously sampled through a hole on the side of the reactor into a vacuum chamber containing a photoionization mass spectrometer. A xenon lamp (E = 8.44 eV) with a sapphire window was used to ionize the radical for mass spectrometric detection.

In a typical bimolecular reaction rate coefficient determination, the radical decay rate was measured in real time at four or five different oxygen concentrations. A single-exponential function $[R] = A + [R]_0 \exp(-k't)$ was fitted to the decay signals. Here, k' is the pseudo-first-order rate coefficient, t is the time, A is the signal background, $[R]$ is a value proportional to the radical concentration, and $[R]_0$ is a value proportional to the radical concentration at t = 0. The pseudo-first-order rate coefficient is defined as $k' = k_w + k[O_2]$, where k is the bimolecular reaction rate coefficient and k_w is the wall reaction rate. The wall reaction rate is the decay rate of the radical without added oxygen and it was typically measured in the beginning and the end of each bimolecular reaction rate coefficient measurement. The obtained pseudo-first-order rate coefficients are then plotted as a function of $[O_2]$ and the slope of a linear fit made to this plot gives the bimolecular rate coefficient. An example of a bimolecular plot is given in Figure 1.

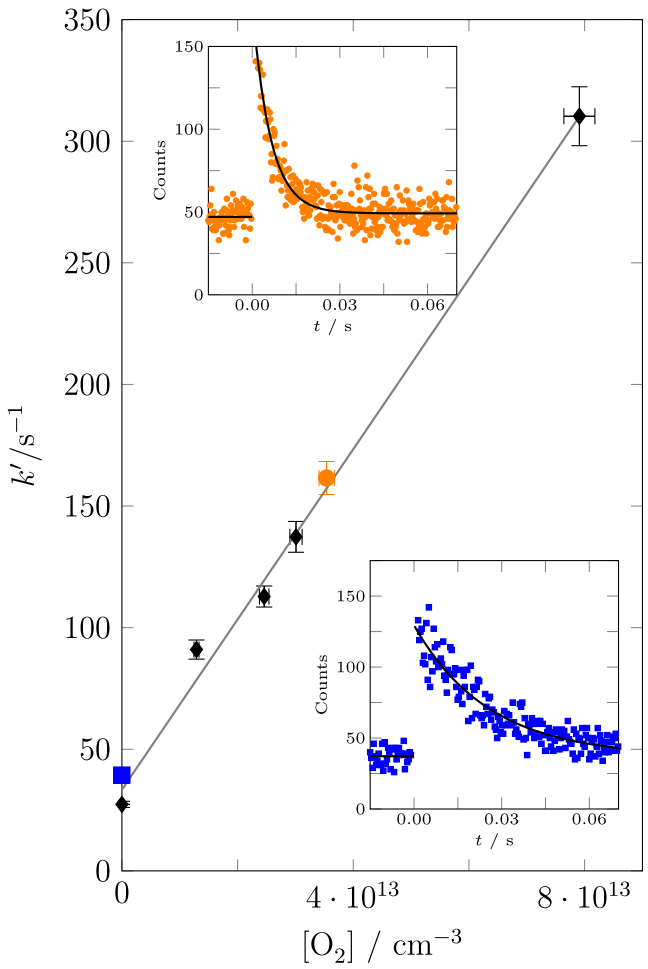

Figure 1. Bimolecular plot to determine the bimolecular rate coefficient of pent-1-en-3-yl + O_2 at m/z = 69 and at T = 298 K and p = 0.18 Torr. Radical decay signals in the absence (blue square) and presence (orange circle) of oxygen are shown in the bottom right corner and top left corner, respectively.

DOI: 10.1021/acs.jpca.9b03923
J. Phys. Chem. A 2019, 123, 7897−7910

Under conditions where the dissociation reaction back to the reactants becomes significant, the above procedure can no longer be applied because the decay profiles are not single-exponential. Now the radical signal decays due to the reactions

$$R + O_2 \underset{k_b}{\overset{k_f}{\rightleftharpoons}} RO_2 \xrightarrow{\delta} \text{products} \quad (3)$$

$$R \xrightarrow{k_w} \text{products} \quad (4)$$

and a double exponential function

$$[R] = A + B\exp(-\lambda_1 t) + C\exp(-\lambda_2 t) \quad (5)$$

needs to be used instead. Here, A is the signal background and B, C, λ_1, and λ_2 are fitting parameters. Knyazev and Slagle[19] derived expressions to obtain the forward rate coefficient (k_f), the backward rate coefficient (k_b), and the unimolecular rate coefficient for further reaction of the R + O_2 association product (δ) using the double-exponential fitting parameters and the separately measured wall reaction rate (k_w). The forward and reverse rate coefficients can then be used to determine the equilibrium constant (gases assumed to be ideal and their standard states chosen as pure gas at 1 bar at the temperature of interest). Examples of the measured radical decay signals are shown in the subfigures of Figure 1 and in Figure 2 for various O_2 concentrations and temperatures,

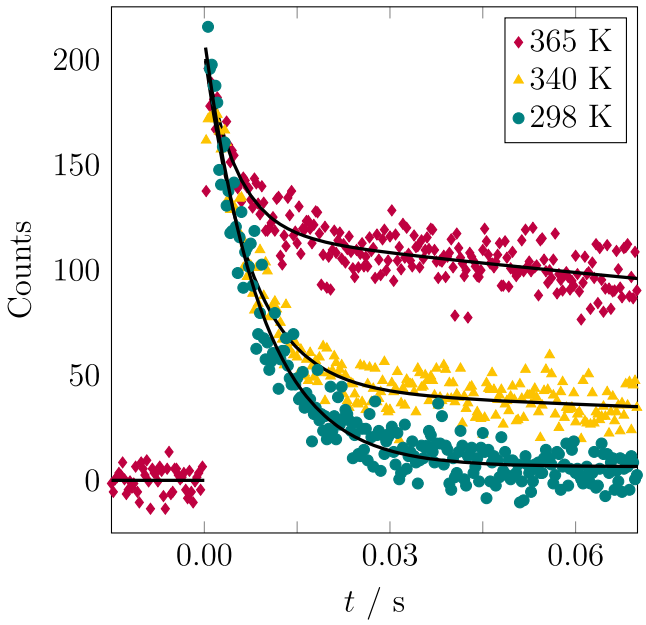

Figure 2. Radical decay signals as a function of temperature and increasing importance of RO_2 decomposition back to the reactants, as embodied in the value of k_b.

respectively. The fitted radical decays are shown as solid black lines. Figure 2 shows how the behavior of the radical decay signal changes as the dissociation reaction back to the reactants becomes important.

In the following discussion, the terms terminal ($R1O_2$) and nonterminal ($R3O_2$) will be used to discriminate between the two potential O_2 association sites of the pent-1-en-3-yl radical. Note that in the experiments the time-resolved behavior of the radical signal was monitored, and consequently, the experiments could not discriminate between the two association channels.

Comparison of Bromide and Chloride Precursors. The majority of our experiments were conducted using the bromide precursor. Because of the smaller bond dissociation energy of carbon-bromide bonds compared to carbon-chloride bonds (66.9 vs 80.8 kcal/mol),[23] the products of bromide precursor photofragmentation are expected to hold more internal energy than the photofragmentation products of the chloride precursor. In order to estimate the amount of vibrational excitation of the pent-1-en-3-yl radical directly after formation, the precursor photofragmentation energetics (electronic energy + zero-point energy) and subsequent isomerization energetics of the pent-1-en-3-yl radical were calculated at the G4//MN15/def2-TZVP[24,25] level of theory using the Gaussian software package[26] (cf. Figure 3).

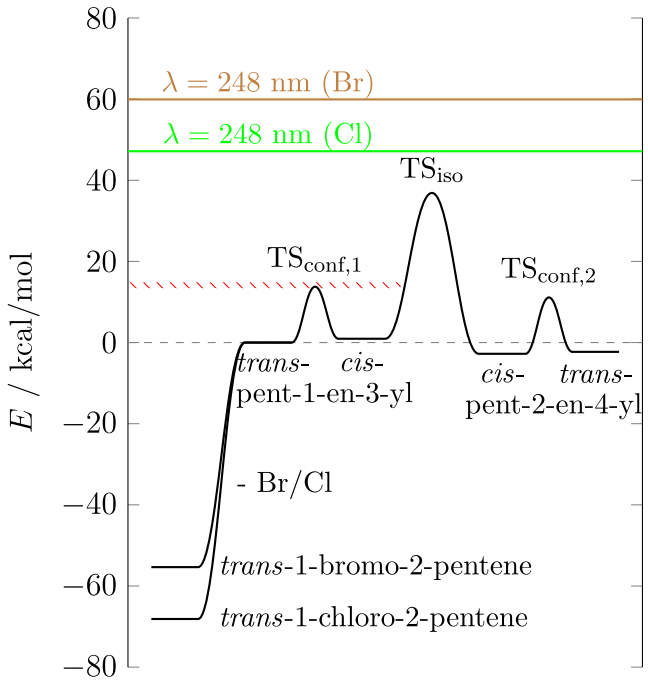

Figure 3. Precursor photofragmentation and pent-1-en-3-yl radical isomerization PES at the G4//MN15/def2-TZVP level of theory. The red, shaded area indicates the estimated excitation of the pent-1-en-3-yl radicals after photofragmentation of *trans*-1-bromopent-2-ene and *trans*-1-chloropent-2-ene at 248 nm wavelength.

When a precursor molecule absorbs a photon with an energy corresponding to 248 nm wavelength, it undergoes simultaneous electronic and vibrational excitation (vibronic transition). While the vibrational excitation can be assumed to be equally distributed among all the internal degrees of freedom of the precursor, the electronic excitation leads to a highly repulsive interaction between the carbon and the halogen atom.[27,28] It has been shown that this repulsive potential leads to a strongly localized vibrational excitation in the polyatomic fragment,[27,28] translational excitation of both fragments, and a large part is consumed by the bond cleavage and does not add to the internal energy of the fragments. Van Veen et al.[27] studied the photofragmentation of methyl bromide and found that the CH_3 umbrella motion of the methyl fragment was vibrationally excited (n = 3). Transferring this to the umbrella motion of the terminal CH_2 group of the pent-1-en-3-yl radical

DOI: 10.1021/acs.jpca.9b03923
J. Phys. Chem. A 2019, 123, 7897−7910

($\vartheta_{umbrella}$ = 2.4 kcal/mol) gives an energy of $n \cdot \vartheta_{umbrella}$ = 7.2 kcal/mol.

The vibrational excitation of the initial vibronic transition is the difference between the total photon energy (248 nm = 5 eV) and the energy of the electronically excited state. The electronic excitation energies of the bromide and chloride precursors were calculated at the TD/TDA-B2PLYP/def2-TZVP level of theory using the ORCA software package.[29] Grimme and Neese[30] reported an uncertainty of 0.32 eV for singlet−singlet excitations of organic compounds using the aforementioned method. Note that this uncertainty is for nonhalogenated compounds. The electronic excitation energies of the bromide and chloride precursors were corrected based on the difference between the calculated and experimental values for methyl bromide (4.94 eV[28,31]) and methyl chloride (5.17 eV[32]), respectively. This procedure gives the electronic states 4.66 and 4.73 eV above the ground state for the bromide and chloride precursors, respectively. Therefore, the vibrational excitation due to the initial vibronic transition amounts to 0.34 eV (7.8 kcal/mol) for the bromide precursor and 0.27 eV (6.2 kcal/mol) for the chloride precursor.

The total vibrational excitation of the pent-1-en-3-yl radicals after photofragmentation is estimated to be 15.0 and 13.4 kcal/mol for the bromide and chloride precursors, respectively. From this estimation, we conclude that the vibrational excitation of the pent-1-en-3-yl radical is similar for both precursors and is well below the isomerization transition structure to the pent-2-en-4-yl radical.

COMPUTATIONAL METHODS

Molecular structures, harmonic frequencies, and one-dimensional-hindered rotor profiles were calculated at the RIJK-B2PLYP-D3BJ/def2-TZVP level of theory.[33,34] The def2-TZVP basis set is chosen as a compromise between the convergence of the MP2 part in the double-hybrid density functional theory (DFT) method and computational cost. While being larger than the TZVP basis set, the def2-TZVP basis set is comparable in size with the 6-311++G(d,p) and the aug-cc-pVDZ basis sets, but computationally less costly than the larger cc-pVTZ basis sets. Single-point energy calculations were carried out at the DLPNO-CCSD(T)/CBS[35,36] and G4[24] levels of theory. The complete basis set (CBS) limit is estimated from aug-cc-pVTZ and aug-cc-pVQZ basis set calculations using the relation[37]

$$E_{CBS} = (4^3 \cdot E_{QZ} - 3^3 \cdot E_{TZ})/(4^3 - 3^3) \quad (6)$$

The Gaussian software package[26] was used for the G4 calculations and the ORCA software package[29] was used for the rest of the calculations.

The R + O_2 association potential was scanned with a step size of 0.05 Å for the terminal and nonterminal association sites at the RIJK-B2PLYP-D3BJ/def2-TZVP level of theory. For each point along the association potential, additional doublet and quartet SC-NEVPT2[38](9,7)/def2-TZVP calculations were performed to calculate the doublet/quartet-splitting as proposed by Goldsmith et al.[39]

$$E = E^{quartet}_{B2PLYP} + (E^{doublet}_{NEVPT2} - E^{quartet}_{NEVPT2}) \quad (7)$$

Schapiro et al.[40] showed that NEVPT2 and CASPT2 give very similar results if the IPEA shift is used for CASPT2. NEVPT2, however, is computationally less demanding and avoids the use of an empirical correction, which has been shown to be problematic in some cases.[41] The active space included the two O_2 triplet electrons and two lone pairs (6 electrons, 4 orbitals), and one electron and one orbital for each carbon atom in the resonance-stabilized system of pent-1-en-3-yl. The obtained association potentials for R + O_2 are discussed in more detail in the Results and Discussion section. Briefly, the association potentials were used as the input in the phase space theory (PST)-based kinetic calculations developed by Pechukas and Light,[42] to compute microcanonical rate coefficients for the R + O_2 → RO_2 reaction. The PST has known limitations in the description of rotational hindrance along the reaction coordinate, as it assumes free-relative rotation between the two reacting fragments. While this simple kinetic theory gives a fundamentally interesting reference, PST should not be used as a purely predictive tool. Instead, it will be used here to estimate the general trend of R + O_2 reactivity, which will then be adjusted via fitting to experimental data to obtain a more reliable description of the rate coefficient. Note that the extrapolative capacity of this combined approach is unknown at this point.

Because variations in the PST parameters did not allow to reproduce the experimental data, a modification of the PST number of states is proposed empirically. By energy-shifting and rescaling the PST number of states $N_{PST}(E)$ by E_{shift}, we managed to achieve a very good fit of the experimental data. The rescaling ensures that the number of states at the energy used for shifting remains unchanged, and thus depends solely on E_{shift}. We used the following equation for adjusting the number of states

$$N_{modified}(E) = N_{PST}(E + E_{shift}) \cdot \frac{N_{PST}(E_{shift})}{N_{PST}(E_{shift} + E_{shift})} = N_{PST}\left(\frac{E + E_{shift}}{2}\right) \quad (8)$$

in which $N_{PST}(E) = c \cdot E^m$, with c and m being functions of the PST parameters provided in the following section.

The Rice−Ramsperger−Kassel−Marcus theory (RRKM)/master equation (ME) simulations were carried out using the MESS software package.[43] Collisional energy transfer was modeled via the Lennard-Jones (LJ) collision frequency model and the exponential-down model

$$\langle \Delta E \rangle_{down} = \langle \Delta E \rangle_{down,0} \cdot \left(\frac{T}{300\ K}\right)^n \quad (9)$$

with n = 0.77 and an initial value for $\langle \Delta E \rangle_{down,0}$ = 200 cm^{-1}, which is adjusted to the experimental data later. The LJ parameters for pent-1-en-3-yl peroxy were obtained via two different approaches: first, via the group additivity theory as implemented in the RMG software package[44] (ε = 300 K and σ = 6.3 Å). Second, via analogy to ethyl acetate[45] (ε = 521 K and σ = 5.2 Å). The LJ parameters of the bath gas (helium) were taken from Hippler et al.:[46] ε = 10.0 K and σ = 2.6 Å.

In order to overcome the uncertainties associated with the theoretical predictions and the limited range of experimental conditions, both results are combined to narrow down the predicted molecular properties used in the ME simulations. The following 10 parameters are considered for optimization: the two $\langle \Delta E \rangle_{down}$ parameters, the two LJ parameters for pent-1-en-3-yl, the two RO_2 well depths, and the four parameters used to solve the phase space integral for R + O_2 → RO_2. The remaining parameters are left unaltered.

DOI: 10.1021/acs.jpca.9b03923
J. Phys. Chem. A 2019, 123, 7897−7910

Initially, a sensitivity analysis is conducted to understand which predictions are affected by which parameters. For this, each parameter is varied by 20% and the sensitivity of the forward and backward R + O_2 rate predictions to these changes is calculated as $dk/k \cdot \Theta/d\Theta$, in which Θ represents the respective parameter. As will be discussed below, this analysis suggests a two-step procedure: first, the experimental equilibrium constant is used to adjust the two RO_2 well depths; second, the collisional energy transfer and the PST description are adjusted to resemble the experimental R + O_2 rate coefficient. For the first step, both RO_2 well depths are altered equally to maintain the original branching ratios. This constraint is imposed based on the assumption that theoretical branching ratios are less uncertain than the respective reaction rates due to partial error cancellation (cf. Supporting Information).

RESULTS AND DISCUSSION

R + O_2 Association Potentials. Previous experimental and theoretical studies have made conflicting statements about the existence of a barrier for O_2 addition to resonance-stabilized radicals, although experimental evidence clearly points toward barrierless O_2 addition.[7,9,12,13,16] This work contributes to this topic with a detailed investigation of pent-1-en-3-yl + O_2 association potentials. Single-reference B2PLYP and multireference NEVPT2 levels of theory were used to see if there is a barrier for O_2 addition in the studied reaction system. The association potentials are shown in Figure 4.

For both R + O_2 association channels, the single-reference B2PLYP method predicts a barrier of 2−3 kcal/mol. At the NEVPT2 level of theory, however, the barrier heights are negligibly small and the barrier positions shift toward larger relative positions. The doublet/quartet-splitting[39] corrected B2PLYP potential energy profiles are considered most accurate and indicate that O_2 addition is barrierless for pent-1-en-3-yl. This observation is in agreement with the sophisticated theoretical and experimental study on the propargyl + O_2 reaction in helium droplets by Moradi et al.[13] Because the allyl + O_2 reaction is almost three times faster than the propargyl + O_2 reaction at room temperature,[12,47] it is reasonable to conclude that the O_2 association with allyl-type radicals is barrierless as well.

The doublet/quartet-splitting corrected B2PLYP association potential is used as basis for phase-space integration according to Pechukas and Light.[42] The implementation of this methodology in the MESS software package requires a power-law description of the potential energy profile. Therefore, the corrected B2PLYP results are fitted using the following equation

$$E = -a/r^b \tag{10}$$

with a and b being fitting parameters. The small bump in the potential energy profiles causes uncertainty in the fitting and stems from the long-range interactions between the two fragments. This prereaction van der Waals complex is submerged and does not need to be separately accounted for.

Potential Energy Profile. The stationary points on the potential energy surface (PES) of the pent-1-en-3-yl + O_2 reaction system involving all the RO_2 to QOOH isomerization transition structures is given in Figure 5 and Table 1. Note that the RO_2 well depths are the unaltered values obtained at the DLPNO-CCSD(T)/CBS level of theory. The well depth adjustments will be discussed in the Parameter Optimization section. The TS and product numbering TS_{ij} and Q*ij*OOH is based on the O_2 association site index (i = 1 or 3) and the internal hydrogen abstraction site (j = 1−5) in a consistent manner, that is, Q35OOH is produced through TS_{35}.

(a) O_2 association with terminal pent-1-en-3-yl site

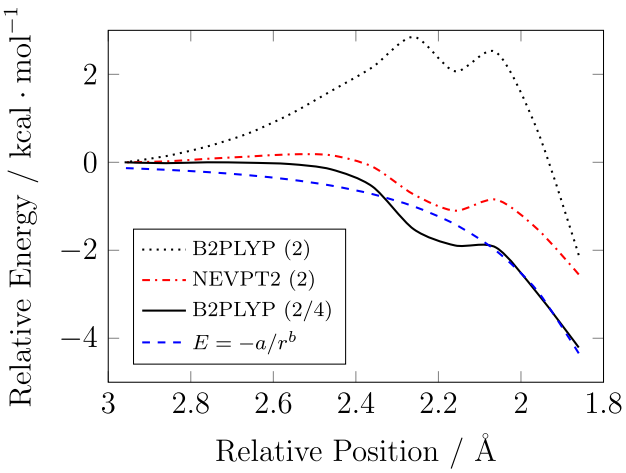

(b) O_2 association with non-terminal pent-1-en-3-yl site

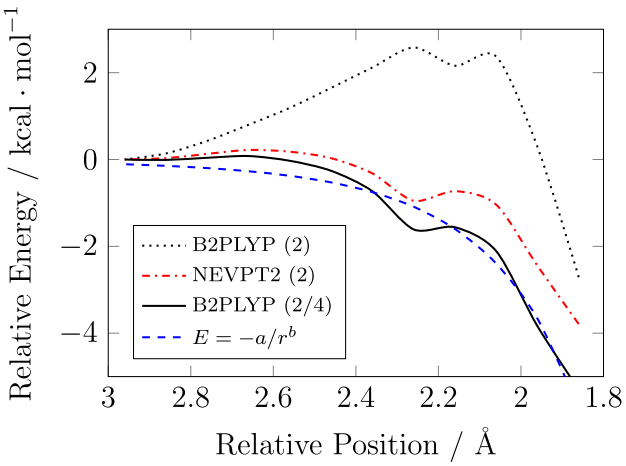

Figure 4. R + O_2 association potentials at the B2PLYP, NEVPT2, doublet/quartet-splitting-corrected B2PLYP levels of theory, and fits to the latter.

The relative G4 and DLPNO-CCSD(T) energies listed in Table 1 show striking agreement, except for the RO_2 well depths. The DFT and G4 levels of theory suffer from substantial uncertainties for predicting the RO_2 well depths (≈4.1, 3.3, and 2.7 kcal/mol for the B3LYP, B2PLYP, and G4 levels of theory, respectively). Moreover, the DFT levels of theory severely underpredict the barrier heights for the formation of Q12OOH, Q32OOH, and Q34OOH. It would appear that compound methods, such as G4, show shortcomings in calculating the energies of resonance-stabilized structures, and more sophisticated methods need to be used instead.

The reactants, R and O_2, are shown in the middle of Figure 5. The barrierless R + O_2 association reactions produce the two

DOI: 10.1021/acs.jpca.9b03923
J. Phys. Chem. A 2019, 123, 7897−7910

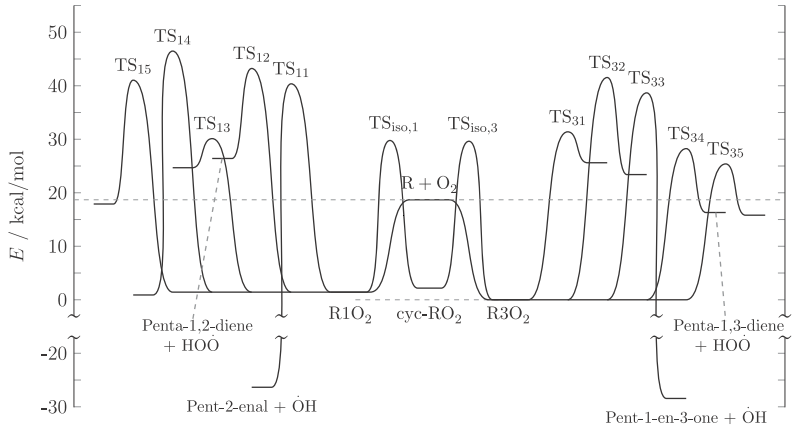

Figure 5. Potential energy profile of the pent-1-en-3-yl + O_2 reaction system. The zero-point energy-corrected DLPNO-CCSD(T)/CBS potential energies used for plotting are given in Table 1. Products without labels are stable QOOH compounds.

Table 1. Potential Energies[b] in kcal/mol at Single-Hybrid DFT, Double-Hybrid DFT, G4, and DLPNO-CCSD(T) Levels of Theory[a]

	B3LYP	B2PLYP	G4	DLPNO-CCSD(T)[c]	product	k/s^{-1}, 298 K, 1 bar	k/s^{-1}, 650 K, 10 bar
R + O_2	14.05	15.17	21.70	18.69			
R1O_2	0.37	0.91	2.09	1.43			
R3O_2	0.00	0.00	0.00	0.00			
cyc-RO_2	6.02	4.44	2.74	2.18			
$TS_{iso,1}$	27.96	30.31	29.86	29.77	cyc-RO_2	5.7×10^{-11}	2.2×10^{0}
$TS_{iso,3}$		30.87	29.62	29.63	cyc-RO_2	$3.7 \times 10-^{11}$	2.5×10^{0}
TS_{11}	38.17	39.95	41.50	40.36	pent-2-enal + ȮH	$2.2 \times 10-^{14}$	5.9×10^{-4}
TS_{12}	35.91	37.84		43.23	penta-1,2-diene + HOȮ	1.5×10^{-22}	5.5×10^{-6}
TS_{13}	28.34	29.66	29.79	30.12	Q13OOH	unstable	unstable
TS_{14}	41.69	43.48	45.71	46.48	Q14OOH	9.1×10^{-19}	1.9×10^{-8}
TS_{15}	37.84	39.45	39.98	41.04	Q15OOH	3.8×10^{-16}	6.6×10^{-6}
TS_{31}	31.29	31.96	30.79	31.39	Q31OOH	2.1×10^{-12}	1.6×10^{-1}
TS_{32}	34.11	35.93	40.30	41.54	Q32OOH	8.5×10^{-21}	5.3×10^{-5}
TS_{33}		38.94	39.20	38.67	pent-1-en-3-one + ȮH	1.1×10^{-13}	4.7×10^{-3}
TS_{34}	19.46	21.91	29.66	28.25	penta-1,3-diene + HOȮ	2.1×10^{-9}	2.4×10^{1}
TS_{35}	24.24	25.24	24.92	25.39	Q35OOH	3.9×10^{-6}	3.3×10^{2}
pent-2-enal + O•H			−26.35				
penta-1,2-diene + HOO•			26.41				
Q13OOH			24.68				
Q14OOH			0.90				
Q15OOH			17.90				
Q31OOH			25.61				
Q32OOH			23.40				
pent-1-en-3-one + O•H			−28.44				
penta-1,3-diene + HOO•			16.31				
Q35OOH			15.81				

[a]For any index *ij*, the first number *i* defines the R*i*O_2 reactant of the TS/product. [b]Sum of single point energies and zero point energies (relative to R + O_2). [c]Zero point energies are taken from B2PLYP/Def2TZVP calculations.

RO_2 adducts, R1O_2 and R3O_2. Molecular oxygen association with the nonterminal site of pent-1-en-3-yl is energetically favored, which would be expected due to the stabilizing effect of the neighboring ethyl group.[48] We could not find a transition state for direct isomerization from the terminal (R1O_2) to the nonterminal (R3O_2) adducts, but both have isomerization pathways to the same five-membered cyclic RO_2 compound (cyc-RO_2). This cyclic RO_2 compound acts as an intermediate in the two-step isomerization between R1O_2 and R3O_2. Because the barriers for these pathways are more than 10 kcal/mol above the reactant energy, isomerization from one to the another RO_2 adduct via cyc-RO_2 is very unlikely. Instead, either the RO_2 adduct would rather dissociate and recombine to the other RO_2 adduct, potentially through a roaming channel.

The dissociation/isomerization of RO_2 via internal hydrogen abstraction can proceed via five channels for each RO_2. The energetically most accessible channel is internal hydrogen abstraction from the terminal methyl group of R3O_2 leading to Q35OOH, with a barrier height of 6.70 kcal/mol above the entrance energy (25.39 kcal/mol total barrier height). We were unable to observe this isomerization channel experimentally in the studied temperature range (T < 365 K). At engine-relevant conditions, however, the high concentration of molecular

DOI: 10.1021/acs.jpca.9b03923
J. Phys. Chem. A 2019, 123, 7897−7910

oxygen could press $R3O_2$ toward Q35OOH, enable a second O_2 addition and/or Q35OOH decomposition. This will be tested with numerical simulations of the pent-1-en-3-yl + O_2 reaction system in the present study. These simulations will be for 650 K, for which the Q35OOH rate coefficient is eight orders of magnitude larger than at standard conditions (cf. Table 1). The second lowest barrier is for the reaction of $R3O_2$ to penta-1,3-diene + HOȮ. For the formally direct R + O_2 to the penta-1,3-diene + HOO$^\bullet$ reaction, the $R3O_2$ species acts as an intermediate structure and the rate coefficient is that of the well-skipping reaction. The formally direct HOO$^\bullet$ elimination rate coefficient is in reasonable agreement with the analogous reaction of the allyl radical with O_2 at 298 K: 1.1×10^{-21} cm^3 s^{-1} versus 2.7×10^{-22} cm^3 s^{-1}.[49] Interestingly, the rate coefficient for nondirect (i.e., $R3O_2$-based) penta-1,3-diene + HOO$^\bullet$ formation increases by 10 orders of magnitude from standard conditions to 650 K, thus two orders of magnitude stronger than the Q35OOH pathway. The stronger temperature-dependence of the penta-1,3-diene + HOO$^\bullet$ pathway compared to the Q35OOH pathway is due to the two fragments (penta-1,3-diene + HOO$^\bullet$) being entropically favored over one (Q35OOH). Internal hydrogen abstractions from the hydrocarbon sites of $R1O_2$ are energetically unfavorable.

The barrier heights for internal hydrogen abstraction from the vinylic and allylic sites in $R1O_2$ and $R3O_2$ show similar trends: abstraction from the vinylic site neighboring the O_2 association site has a much higher barrier than abstraction from the other ("far") vinylic site. Moreover, the latter internal hydrogen abstraction barrier is smaller than the barrier for abstraction from the O_2 association site, although being an allylic site. This is due to the TS being a three-membered ring, which are typically energetically less favorable than the six-membered TS rings for the "far" vinylic abstraction sites.

Notably, the six-membered $R1O_2$ to the Q13OOH transition structure (hydrogen abstraction from the vinylic site) is energetically much more favored over the seven-membered $R1O_2$ to the Q14OOH transition structure (allylic site). This is somewhat unintuitive, as allylic hydrogens are usually weaker bound than vinylic hydrogens,[50] but the reason for this is the high tension acting on the C=C double bond in the seven-membered TS ring, resulting in visible distortion of the sp^2-hybridized carbons (cf. Supporting Information). This has implications for detailed kinetic modeling, as Westbrook et al.[2] has stated that alkylperoxy radical isomerization reactions with a C=C double bond within the TS ring are of particular importance to the kinetic modeling of unsaturated hydrocarbon fuels.

Note that in the ME model, we have not included dissociation channels for the QOOH species because these channels are practically irrelevant at the present experimental conditions. When comparing the $k_{298\,K,1\,bar}$ values in Table 1, it becomes clear that Q35OOH formation is orders of magnitude faster compared to the competing internal hydrogen abstraction reactions. For Q35OOH, we included an irreversible sink in order to approximately account for the effect of a second O_2 addition on the rate predictions (pseudo-first-order rate coefficient estimated as $k_{Q35OOH+O_2} = 10^{-12}$ cm^3 s^{-1}·[O_2]).

The size of the TS-ring for internal hydrogen abstraction not only affects the barrier height, but also the entropy. The larger the ring, the more internal rotors are lost. As a consequence, the entropic barrier is larger and the rate coefficient is smaller. When replacing the lost internal rotors with harmonic oscillators, for example, in the reaction of $R3O_2$ to Q35OOH, the rate coefficient at 298 K and 1 bar increases by a factor of 2.6. This is due to the lower energy level density for the harmonic oscillators compared to the internal rotors, resulting in a lower stability, thus higher reactivity.

Parameter Optimization. First, the sensitivities of the theoretical R + O_2 ⇌ $R1/3O_2$ reaction rate coefficients to the 10 aforementioned RRKM/ME parameters are evaluated: the two RO_2 well depths, the four parameters describing the R + O_2 association potentials, and the four parameters describing the collisional energy transfer. The rate coefficient sensitivities at 243 K and 1.03 Torr are presented in Figure 6. The experimental results are provided in Tables 2 and 3.

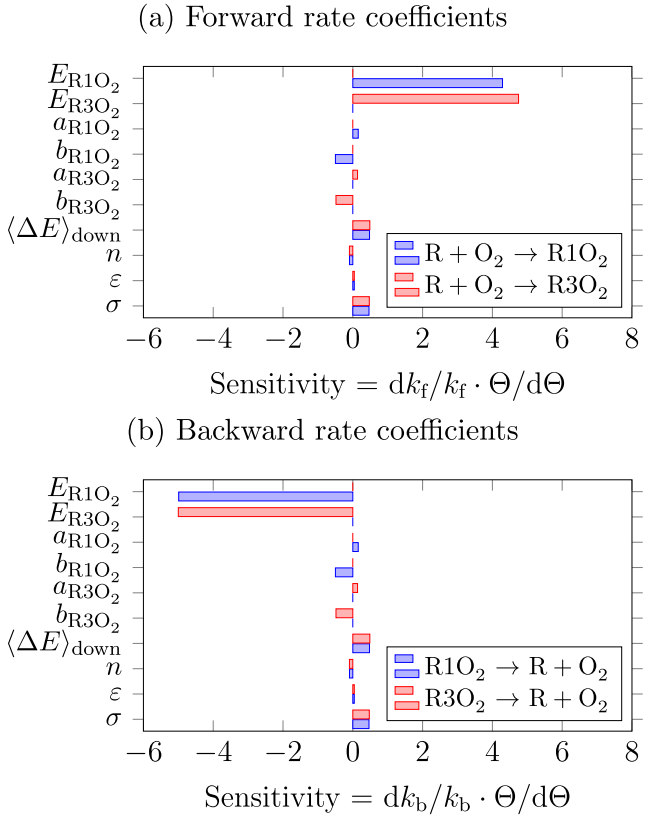

Figure 6. R + O_2 ⇌ RO_2 rate coefficient sensitivities at T = 243 K and p = 1.03 Torr to the 10 aforementioned parameters (represented via Θ in the formula).

The forward and backward rate coefficients of the R + O_2 ⇌ $R1/3O_2$ reactions are highly sensitive to the RO_2 well depths. The theoretical equilibrium constants, however, are solely sensitive to the RO_2 well depths and insensitive to the remaining eight parameters by definition. Therefore, the experimental equilibrium constant data can be used to optimize the well depths independently of the other adjustable parameters. As a consequence, the experimental equilibrium constant gives valuable information about the reliability of the calculated DLPNO-CCSD(T)/CBS energies. The well depths are changed in equal measure to keep the branching ratio between the two association channels approximately constant. As mentioned above, this constraint is imposed based on the

DOI: 10.1021/acs.jpca.9b03923
J. Phys. Chem. A 2019, 123, 7897−7910

Table 2. Experimental Conditions and Results for the Pent-1-en-3-yl + O_2 Bimolecular Rate Coefficient Measurments[a]

T (K)	p_{He}[b] (Torr)	[He]/10^{16} (cm^{-3})	[precursor]/10^{11} (cm^{-3})	[O_2]/10^{13} (cm^{-3})	k' (s^{-1})	k_W[c] (s^{-1})	k_W[d] (s^{-1})	k/10^{-14} (cm^3 s^{-1})
				***trans*-1-Bromopent-2-ene**[h]				
198	0.18	0.862	9.23	1.29−7.91	91.0−310	33.4 ± 1.40	35.3 ± 4.00	347 ± 11
198	0.36	1.75	6.10	1.19−3.06	63.0−140	16.5 ± 1.45	16.8 ± 5.88	360 ± 30
198	0.36	1.76	7.87	1.61−4.38	108−175	41.7 ± 1.90	46.3 ± 6.05	314 ± 23
198	0.77	3.74	7.92	1.11−2.71	118−183	53.3 ± 1.78	57.6 ± 5.28	463 ± 30
243	0.21	0.847	31.1	4.90−20.2	77.9−287	7.64 ± 0.46	12.8 ± 4.80	137 ± 4
243	0.46	1.83	30.0	2.49−9.43	53.6−170	5.92 ± 0.53	7.06 ± 1.97	170 ± 4
243	0.95	3.78	31.2	2.28−7.47	58.5−158	9.46 ± 0.49	11.2 ± 0.49	204 ± 7
243	1.40	5.55	29.6	2.14−7.98	61.4−201	8.27 ± 0.49	8.07 ± 3.11	235 ± 7
243[e]	2.30	9.13	23.0	2.55−6.10	88.7−163	16.8 ± 1.63	22.5 ± 10.3	263 ± 30
243[e]	3.60	14.3	15.0	1.79−4.50	106−210	25.4 ± 2.46	24.5 ± 9.07	395 ± 37
243[e]	3.62	14.4	52.4	2.79−5.58	141−216	62.6 ± 9.23	62.2 ± 5.34	280 ± 16
267	0.24	0.869	7.36	2.41−7.52	25.9−81.2	5.05 ± 0.64	4.49 ± 1.79	103 ± 4
267	0.51	1.85	7.31	2.30−7.48	32.6−92.1	3.34 ± 0.56	3.82 ± 1.17	120 ± 3
267	1.04	3.74	7.09	1.76−7.31	27.6−113	3.68 ± 0.50	3.43 ± 1.42	150 ± 3
298	0.27	0.882	5.95	10.4−51.1	64.8−309	0.07 ± 3.56	7.11 ± 1.47	60.0 ± 1.2
298	0.57	1.85	4.30	2.30−11.8	18.1−94.7	1.14 ± 0.60	0.86 ± 1.68	82.0 ± 2.2
298	1.17	3.80	5.70	2.56−9.55	30.9−110	3.82 ± 0.51	3.86 ± 1.49	111 ± 3
298[e]	1.47	4.76	23.7	3.97−17.9	56.8−226	14.2 ± 1.18	13.1 ± 4.54	116 ± 5
298[e]	2.87	9.30	17.1	4.64−11.6	82.0−153	15.0 ± 1.74	17.3 ± 9.71	120 ± 13
298[e]	2.88	9.33	26.7	4.49−10.1	78.7−148	24.9 ± 0.95	24.7 ± 1.77	119 ± 3
298[e]	4.43	14.4	15.7	3.56−9.07	75.8−166	22.2 ± 1.27	21.1 ± 1.57	158 ± 3
298[e]	4.50	14.6	50.8	4.37−9.16	84.9−154	20.2 ± 1.21	21.0 ± 2.34	148 ± 4
304[f]	1.18	3.74	10.8	5.34−17.8	77.4−189	30.6 ± 1.30	30.4 ± 1.30	89.8 ± 1.4
304[f]	1.58	5.03	4.83	2.18−10.6	53.4−134	36.7 ± 1.50	36.2 ± 2.10	95.1 ± 3.5
306[g]	2.81	8.87	19.0	6.21−12.9	108−191	27.2 ± 1.30	27.1 ± 3.70	124 ± 5
				***trans*-1-Chloropent-2-ene**[i]				
304	1.19	3.76	259	3.30−7.74	33.9−71.1	4.32 ± 1.05	4.22 ± 1.35	84.6 ± 2.9
304[g]	2.89	9.19	694	2.20−5.82	31.5−69.1	6.22 ± 1.11	6.66 ± 2.14	111 ± 6

[a]Stated uncertainties are 1σ. A xenon lamp with a sapphire window was used for ionization in all experiments. [b]Reactor: d = 1.7 cm, stainless steel, halocarbon wax coating, unless otherwise stated. [c]Average of measured wall rates. [d]Wall rate determined from the linear fit y-axis intercept. [e]Reactor: d = 0.8 cm, stainless steel, halocarbon wax coating. [f]Reactor: d = 1.7 cm, quartz, boric acid coating. [g]Reactor: d = 0.85 cm, quartz, boric acid coating. [h]Radical precursor: *trans*-1-bromopent-2-ene kept at roughly −5 °C. [i]Radical precursor: *trans*-1-chloropent-2-ene kept at roughly −8 °C.

assumption of partial cancellation of computational errors for branching ratio calculations (cf. Supporting Information).

The experimental equilibrium constant is initially underpredicted by current computations, and to remedy this, the RO_2 well depths are increased (lowered in energy) by 0.26 kcal/mol. This adjustment is well within the methodological uncertainty of <0.7 kcal/mol.[51] The experimental, original theoretical, and energy-corrected theoretical equilibrium constants are given in Figure 7. Note that the averaging scheme proposed by Knyazev and Slagle[19] is used to obtain an average theoretical R + O_2 ⇌ RO_2 equilibrium constant which can be compared to the experimental one.

The lowering of the RO_2 well depths causes overprediction of the R + O_2 rate coefficient, which has to be counteracted by adjusting the remaining parameters. Unsurprisingly, the R + O_2 rate coefficients are sensitive to the PST parameters. As mentioned before, instead of adjusting the parameters used for fitting the R + O_2 addition potentials, we adjust the resulting number of states with a single E_{shift} parameter for both O_2 association channels. With this procedure, we hope to empirically account for the incorrect description of rotational hindrance in the PST formulation. The LJ interaction strength ε and the exponent of collisional energy transfer temperature-dependence n have negligibly small effects on the R + O_2 rate coefficient (cf. Figure 6a) and are left unaltered. The collisional energy transfer at 300 K $\langle\Delta E\rangle_{down,0}$ is included in the optimization and is expected to be in the range from 100 to 200 cm^{-1}.[52] While the R + O_2 rate coefficient is sensitive to the LJ collisional diameter σ, it is not included in the optimization, due to having a very similar effect as $\langle\Delta E\rangle_{down,0}$. Note that any uncertainty in the collisional diameter is compensated by fitting $\langle\Delta E\rangle_{down,0}$, which has a limited physical meaning as a consequence. Instead, we test the RMG-based and analogy-based parameters in two separate optimizations. In the optimization, we aim at minimizing the root-mean-squared-deviation (RMSD) between the predicted and experimental rate coefficient at 198, 243, 267, and 298 K and all measured pressures.

Irrespective of the LJ parameters, optimization yields a number of state energy-shift of $E_{shift} \approx 0.87$ kcal/mol. The collisional energy transfer at 300 K depends on the LJ collisional diameter σ, and amounts to $\langle\Delta E\rangle_{down,0}$ = 100 and 112 cm^{-1} for the RMG-based and analogy-based σ, respectively. Both values for $\langle\Delta E\rangle_{down,0}$ are in the expected range and the final RMSD for both optimizations are the same. For the following rate predictions, we decided to move forward with the analogy-based LJ parameters, due to having a larger $\langle\Delta E\rangle_{down,0}$ (which is likely considered more realistic). The experimental, energy-corrected theoretical, and final adjusted rate coefficients at ≈1 Torr are given in Figure 8. The pressure-

DOI: 10.1021/acs.jpca.9b03923
J. Phys. Chem. A 2019, 123, 7897−7910

Table 3. Experimental Conditions and Results for the Pent-1-en-3-yl + O_2 ⇌ Pent-1-en-3-ylperoxy Equilibrium Constant Measurements[a]

T (K)	p[b] (Torr)	[M]/10^{16} (cm^{-3})	[O_2]/10^{13} (cm^{-3})	k_W[c] (s^{-1})	δ[d] (s^{-1})	k_f[e]/10^{-14} (cm^3 s^{-1})	k_b[f] (s^{-1})	ln(K)[g]
				***trans*-1-Bromopent-2-ene**[i]				
334	1.35	3.90	3.21	22.1 ± 1.1	18.6 ± 6.3	55.5 ± 6.0	21.0 ± 24.7	13.26 ± 1.18
335	1.33	3.83	2.53	20.4 ± 1.4	29.2 ± 9.3	50.8 ± 7.4	25.5 ± 28.1	12.97 ± 1.11
339[h]	3.25	9.25	2.02	12.8 ± 0.6	10.7 ± 1.4	73.8 ± 5.3	50.4 ± 12.8	12.65 ± 0.26
341	1.35	3.82	2.49	21.0 ± 1.3	19.6 ± 5.8	52.4 ± 7.0	36.5 ± 25.9	12.63 ± 0.72
343[h]	3.37	9.48	2.06	12.5 ± 0.6	10.0 ± 1.7	68.4 ± 6.1	62.2 ± 18.2	12.35 ± 0.31
347	0.70	1.95	2.87	18.8 ± 1.4	25.5 ± 11.0	27.7 ± 6.5	31.4 ± 31.0	12.12 ± 1.01
348	1.85	5.13	2.68	21.0 ± 1.1	12.7 ± 3.3	44.6 ± 5.7	56.4 ± 23.8	12.01 ± 0.44
348[h]	3.39	9.40	2.01	15.8 ± 1.2	21.1 ± 5.1	50.4 ± 6.9	47.9 ± 23.4	12.20 ± 0.51
352	1.41	3.85	2.30	20.3 ± 1.0	14.1 ± 5.7	33.2 ± 6.9	67.5 ± 31.3	11.52 ± 0.51
353[h]	3.48	9.51	2.11	12.7 ± 0.7	3.9 ± 1.9	43.0 ± 6.4	113 ± 29	11.26 ± 0.30
358	1.45	3.91	3.80	17.6 ± 1.1	22.5 ± 5.3	36.1 ± 5.9	113 ± 43	11.08 ± 0.41
358	1.47	3.96	6.15	19.5 ± 0.9	13.5 ± 2.7	38.3 ± 4.7	108 ± 45	11.18 ± 0.44
363	1.46	3.89	3.82	18.5 ± 0.8	18.4 ± 6.2	27.2 ± 6.0	143 ± 55	10.54 ± 0.44
363[h]	3.52	9.36	3.82	18.1 ± 1.1	18.9 ± 10.0	39.6 ± 14.3	226 ± 110	10.46 ± 0.61
365	1.47	3.95	4.24	17.2 ± 1.0	15.1 ± 5.4	32.2 ± 7.3	172 ± 71	10.52 ± 0.47
369	1.51	3.96	5.01	17.8 ± 1.3	18.4 ± 14.0	18.3 ± 9.5	205 ± 148	9.77 ± 0.89
370	1.48	3.86	3.80	19.9 ± 0.8	12.2 ± 6.0	23.5 ± 6.8	203 ± 78	10.03 ± 0.48
				***trans*-1-Chloropent-2-ene**[j]				
351	1.86	5.10	3.08	18.2 ± 1.9	26.3 ± 7.9	64.0 ± 1.2	94.3 ± 64.3	11.85 ± 0.71
358	1.90	5.12	6.15	9.75 ± 0.7	9.25 ± 2.60	42.8 ± 6.8	125 ± 42	11.15 ± 0.37
367	1.92	5.06	3.10	11.9 ± 0.7	11.7 ± 5.6	30.1 ± 7.3	215 ± 88	10.23 ± 0.51

[a]A xenon lamp with a sapphire window was used for ionization in all experiments. [b]Reactor: d = 1.7 cm, quartz, boric coating, unless otherwise stated. [c]Average of measured wall rates for pent-1-en-3-yl radical. Stated uncertainties is the average standard error (1σ) of the fits. [d]Irreversible first-order loss for rate pent-1-en-3-ylperoxy radical. Propagation of error used to obtain the uncertainty. [e]Bimolecular rate coefficient for the forward reaction. Propagation of error used to obtain the uncertainty. [f]Unimolecular rate coefficient for the reverse reaction. Propagation of error used to obtain the uncertainty. [g]The standard state of the species is chosen as pure ideal gas at 1 bar at the temperature of interest. Propagation of error used to obtain the uncertainty. [h]Reactor: d = 0.85 cm, quartz, boric oxide coating. [i]Radical precursor: *trans*-1-bromopent-2-ene kept at roughly −5 °C. [j]Radical precursor: *trans*-1-chloropent-2-ene kept at roughly −5 °C.

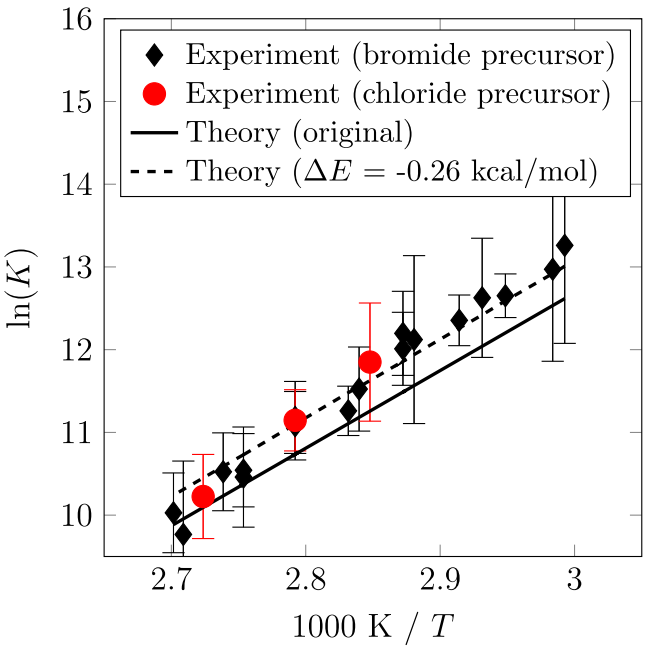

Figure 7. Experimental and theoretical equilibrium constants for the R + O_2 ⇌ RO_2 reaction.

dependent rate coefficients will be discussed in the next section. Note that the experimental rate coefficient is for the total radical consumption, while the theoretical rate coefficient is explicitly for R + O_2 (sum of both channels). For the present low-temperature conditions, however, the experimental radical consumption is dominated totally by the R + O_2 reaction.

RRKM/ME Simulations. The temperature- and pressure-dependent rate coefficient for the pent-1-en-3-yl + O_2 reaction is calculated for the complete range of experimental conditions via RRKM/ME simulations using the aforementioned optimized parameters. The comparison of present experimental and theoretical results is given in Figure 9.

The pressure-dependent fall-off flattens out with increasing pressure and the high-pressure limit is almost reached at around 4 Torr at 198 K (≈85%; cf. solid line in Figure 9). At room temperature (298 K), the high-pressure limit is not reached at 4 Torr (≈42%; cf. dotted line in Figure 9). This temperature-dependent fall-off trend is well-known and observed for other R + O_2 reactions.[53] The modified Arrhenius fits to the final R + O_2 rate coefficients are given in Table 4.

In order to better understand the oxidation of resonance-stabilized radicals, the bimolecular rate coefficient of the pent-1-en-3-yl + O_2 reaction is compared to the R + O_2 reaction rate coefficients of smaller resonance-stabilized radicals. Figure 10 shows the measured and predicted R + O_2 bimolecular rate coefficients for allyl, isobutenyl, and pent-1-en-3-yl. The bimolecular rate coefficient of the allyl + O_2 reaction has been measured by Rissanen et al.[12] and Jenkin et al.[8] at sub- and near-atmospheric pressures. Lee and Bozzelli[7] predicted the allyl + O_2 rate coefficient at an atmospheric pressure. For isobutenyl oxidation, no experimental data is available, but Chen and Bozzelli[16] calculated the high-pressure rate

DOI: 10.1021/acs.jpca.9b03923
J. Phys. Chem. A 2019, 123, 7897−7910

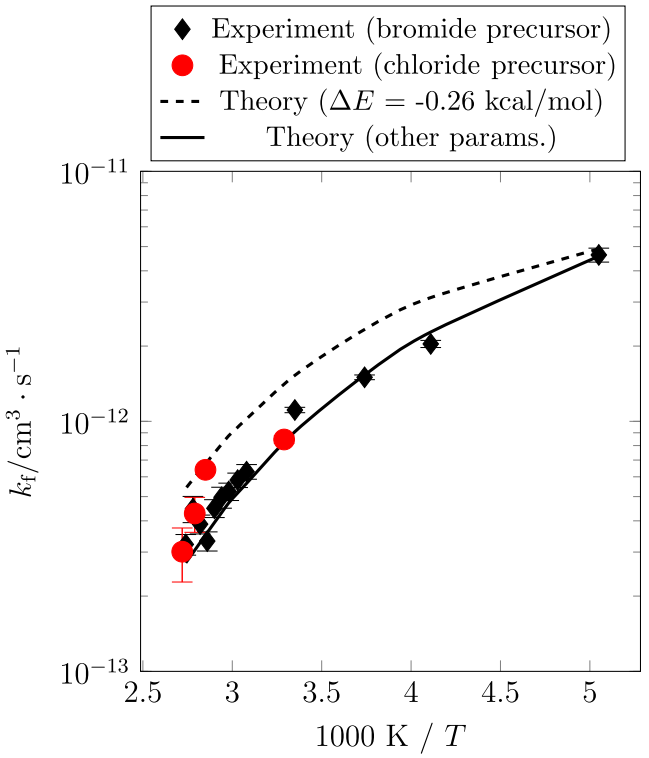

Figure 8. Experimental ($p \approx 1$ Torr, closest experimental pressure for given temperature) and theoretical (p = 1 Torr) R + O_2 rate coefficients with optimized parameters at 1 Torr. Scattering in the experimental data partly results from different pressures (ranging from 0.69 to 1.92 Torr).

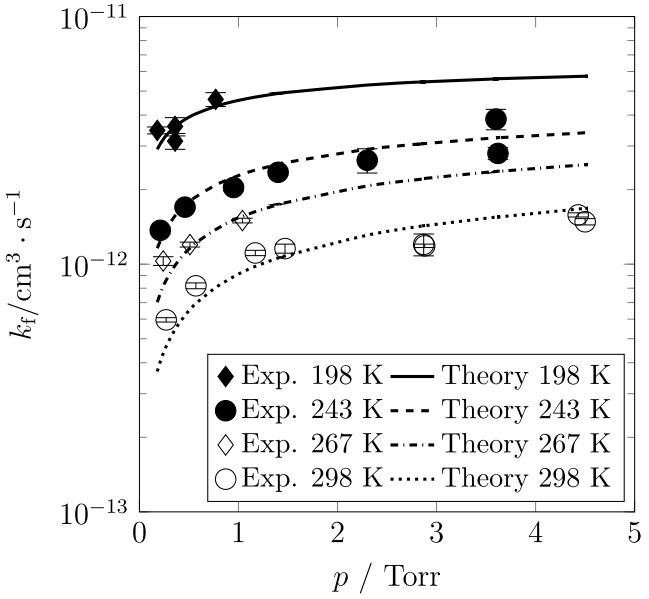

Figure 9. Experimental and theoretical temperature- and pressure-dependent rate coefficients of the pent-1-en-3-yl + O_2 reaction. Helium used as a bath gas.

coefficient. Note that the present predictions at 1 Torr and 1 atm are limited to temperatures below 550 and 650 K, respectively, due to the mixing of collisional and relaxational eigenvalues of the ME above this temperature.[54]

By comparing the measured bimolecular rate coefficient of the pent-1-en-3-yl + O_2 reaction to those measured for the allyl + O_2 reaction,[8,12] one observes slightly higher reactivity for pent-1-en-3-yl + O_2 at low temperatures. The slope of pent-1-en-3-yl + O_2 rate coefficient, however, is steeper, presumably leading to lower reactivity at higher temperatures. The inversion of the slope of the calculated rate coefficient for the allyl + O_2 reaction is due to the ∼1 kcal/mol barrier proposed by Lee and Bozzelli.[7] As a consequence, the predicted allyl + O_2 rate coefficient heavily underestimates the experimental ones at low temperatures.[8,12] The consistency between the present experiments and theory and the similarity between the experimental allyl + O_2 and pent-1-en-3-yl + O_2 rate coefficients (cf. Figure 10) suggest that allyl + O_2 is barrierless, as initially proposed by Bozzelli and Dean.[9] It appears that the ∼1 kcal/mol activation energy reported for allyl + O_2 is an artifact of the previous single-reference calculation, similar to what was observed in the present work.

In contrast to the predicted high-pressure limit of the pent-1-en-3-yl + O_2 reaction, the predicted high-pressure limit of the isobutenyl + O_2 reaction rate coefficient varies significantly with temperature. This results from the ∼1.5 kcal/mol barrier for the isobutenyl + O_2 reaction proposed by Chen and Bozzelli.[16] Assessment of this barrier would either require experimental data for the isobutenyl + O_2 reaction (not available), or a detailed theoretical study of the R + O_2 association potentials (similar to the present study).

Numerical Simulations. In order to evaluate the relevance of pent-1-en-3-yl oxidation chemistry at engine-relevant conditions, the pent-1-en-3-yl + O_2 reaction system is simulated under autoignition circumstances. The initial mixture consists of 10^{15} cm^{-3} pent-1-en-3-yl radicals at t = 0 in air (21% O_2). The initial pressure is 10 bar, which corresponds to $[O_2] = 2.3 \times 10^{19}$ cm^{-3} for isothermal simulation at a temperature of 650 K. This condition is typically engine-relevant for low-temperature ignition. Numerical simulations were carried out using the Cantera software package.[55]

In addition to the rate coefficients for all reactions in Figure 5 obtained from the present RRKM/ME simulations, we included pent-1-en-3-yl radical dissociation,[56] self-recombination (R + R; analogy to C_3H_3 + C_3H_3[10]), Q35OOH dissociation (ring closure, cyclic ether formation, and trimolecular decomposition; cf. Supporting Information for analogy details[57,58]), and second O_2 addition (QOOH + O_2; analogy to Goldsmith et al.[59]). Note that O_2QOOH is modeled as a sink in the present simulations. Therefore, the O_2QOOH concentration profiles are upper bounds of the actual O_2QOOH concentration. The kinetic model can be found in the Supporting Information The concentration profiles of R, O_2QOOH, HOO•, and •OH are shown in Figure 11 with (w/) and without (w/o) a second O_2 association pathway.

More than half of the pent-1-en-3-yl radicals are consumed within the first millisecond of the simulation, mostly via the first O_2 addition. As soon as the R + O_2 ⇌ RO_2 equilibrium is established, the pent-1-en-3-yl radical consumption is dominated by the formally direct R + O_2 → penta-1,3-diene + HOO• reaction. The second most important radical consuming pathway is the formation of Q35OOH and either second O_2 addition (if considered) or dissociation (which yields •OH and a cyclic ether). Notably, about 99% of the radical consumption flux goes through R3O_2-based chemistry, whereas R1O_2-based chemistry is practically irrelevant. The pent-1-en-3-yl radicals are consumed within ≈50 ms.

DOI: 10.1021/acs.jpca.9b03923
J. Phys. Chem. A 2019, 123, 7897−7910

Table 4. Modified Arrhenius ($k(T) = A{\cdot}T^{n}{\cdot}\exp(-E_a/(R{\cdot}T))$) Fits for the R + O_2 Rate Coefficients

pressure (atm)	A ($cm^3{\cdot}s^{-1}$)	n	E_a (cal/mol^{-1})	T range (K)	fit error (%)
		R + O_2 to R1O_2			
inf	2.070×10^{11}	0.105	−701.7	200−1000	0.4
100.0	6.874×10^{18}	−2.433	915.4	200−950	5.6
10.00	5.067×10^{24}	−4.479	1994.2	200−800	7.4
1.000	2.613×10^{32}	−7.223	3278.4	200−700	7.9
0.100	1.476×10^{41}	−10.420	4556.5	200−650	6.8
0.010	8.425×10^{46}	−12.699	5045.0	200−600	4.3
0.001	1.858×10^{49}	−13.878	4825.6	200−550	2.4
		R + O_2 to R3O_2			
inf	1.602×10^{11}	0.139	−706.1	200−1000	0.4
100.0	1.488×10^{19}	−2.551	1004.7	200−950	5.9
10.00	1.585×10^{25}	−4.654	2107.9	200−800	7.7
1.000	9.593×10^{32}	−7.426	3394.7	200−700	8.1
0.100	4.769×10^{41}	−10.610	4651.2	200−650	6.9
0.010	2.048×10^{47}	−12.850	5110.2	200−600	2.4
0.001	3.632×10^{49}	−13.997	4873.8	200−550	2.4

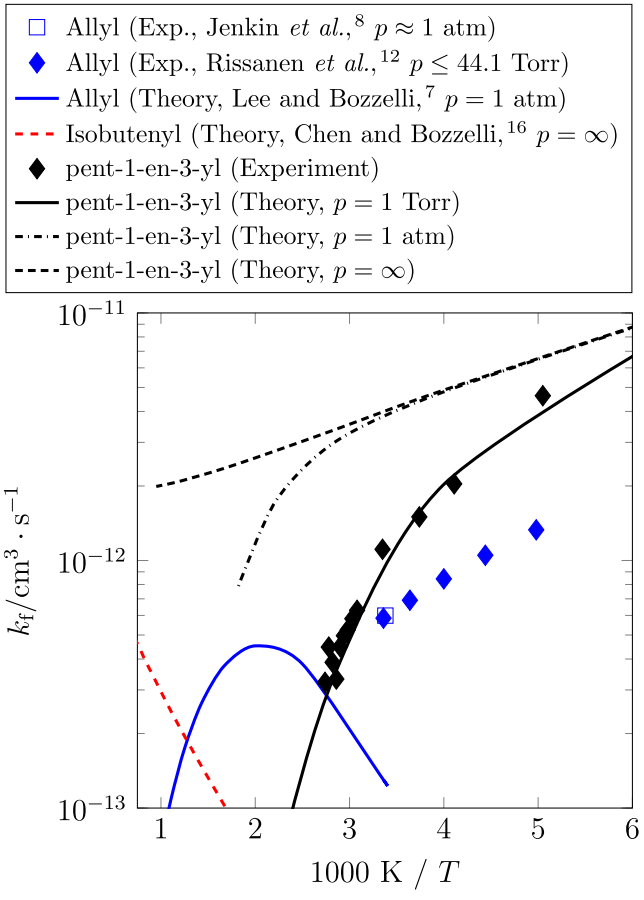

Figure 10. Comparison of allyl, isobutenyl, and pent-1-en-3-yl rate coefficients with molecular oxygen. The allyl + O_2 data was measured by Jenkin et al.[8] and Rissanen et al.,[12] and calculated by Lee and Bozzelli.[7] The isobutenyl + O_2 data was predicted by Chen and Bozzelli.[16]

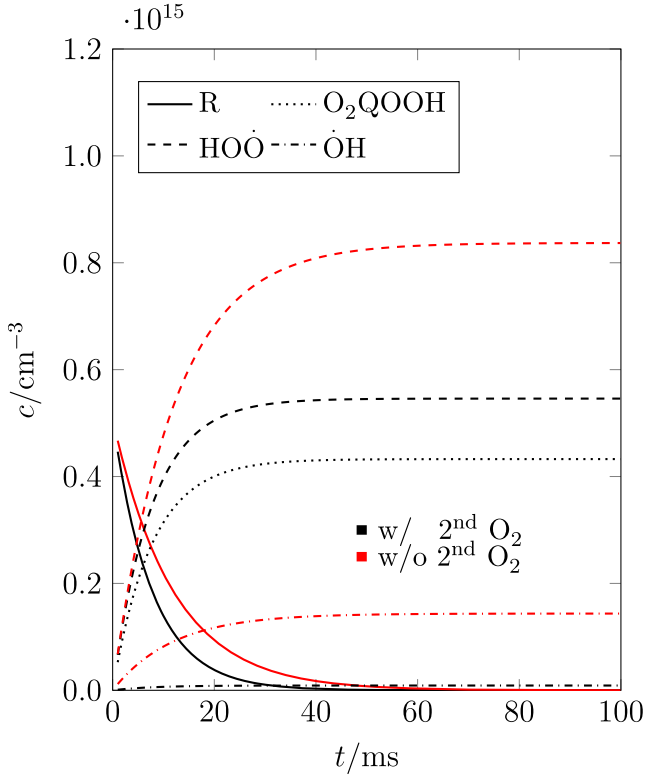

Figure 11. Concentration profiles of the pent-1-en-3-yl radical (R), the second O_2 adduct O_2QOOH, the hydroperoxy radicals (m/z = 101−68), and of the hydroxy radicals (m/z = 101−84) from numerical simulation at 650 K and 10 bar.

The HOO• concentration increases faster than the O_2QOOH or •OH concentrations and dominates the product distributions for both simulations (w/ and w/o second O_2 addition). If the second O_2 addition is not considered (w/o second O_2), Q35OOH dissociation is the only relevant consumption pathway of the RO_2 reaction network. Because this consumption pathway is much slower than the formally direct H-atom abstraction via O_2, the resulting ȮH yield remains small (14%) compared to HOȮ yield (84%; residue is 2% butadiene). If the second O_2 addition is considered (w/ second O_2), Q35OOH rapidly adds to O_2 and the R + O_2 → R3O_2 and R3O_2 → Q35OOH reactions lead to a larger total flux through Q35OOH. Consequently, Q35OOH consumption is dominated by the O_2 addition and the O_2QOOH yield (43%) exceeds the •OH yield in the other simulation (w/o second O_2). Still, the major product is HOO• (55%; residues are 1% butadiene and 1% alternatively produced •OH).

DOI: 10.1021/acs.jpca.9b03923
J. Phys. Chem. A 2019, 123, 7897−7910

The two simulated cases (w/ and w/o second O_2 addition) are the limiting cases for the estimated product distributions. In any case, large amounts of HOO• and penta-1,3-diene are expected, but the second most important product strongly depends on the branching ratio between the second O_2 addition and Q35OOH dissociation. Further calculations and experiments will be conducted to determine the fate of Q35OOH in low-temperature oxidation chemistry.

CONCLUSIONS

The kinetics and thermochemistry of the pent-1-en-3-yl + O_2 reaction have been studied using both experimental and computational methods. The experiments were performed at low temperatures (198−370 K) at subatmospheric pressures. RRKM/ME calculations were then performed and the results were compared with the experiments. The calculations showed that terminal and nonterminal RO_2 adducts are formed at equal rates. However, several of the RRKM/ME parameters had to be adjusted for the model to reproduce the experimental rate coefficient and equilibrium constant data with satisfactory accuracy. These adjustments did not exceed parameter uncertainties. The resulting prediction agrees with experiments within a factor of 1.5. The initial O_2 association reaction was found to be barrierless. It seems increasingly clear from experiments that the O_2 reactions of allyl-type radicals are barrierless and this behavior can be reproduced computationally when accounting for multireference effects. The optimized RRKM/ME model was used to simulate the pent-1-en-3-yl + O_2 reaction at engine-relevant conditions. The model was particularly important in evaluating the relative importance of the two R + O_2 association channels. The addition to the nonterminal carbon was found to be more important under engine-relevant conditions.

The low reaction enthalpy of the O_2 addition makes subsequent reactions of RO_2 toward QOOH less pronounced compared to saturated hydrocarbons. In fact, numerical simulations indicate that most of pent-1-en-3-yl radicals are consumed by a formally direct hydrogen abstraction reaction before the first O_2 addition under typical engine-relevant conditions (pent-1-en-3-yl + O_2 penta-1,3-diene + HOO). However, 14−43% of pent-1-en-3-yl radicals are consumed via pathways involving QOOH radicals, which can undergo a second O_2 addition (chain branching) or decomposition (chain propagation). This is due to the rapid equilibration of the R + O_2 ⇌ RO_2 reaction, resulting in a steady-state concentration of RO_2, which can further isomerize to QOOH.

Our work shows that simple kinetic models (PST) and moderately computationally demanding levels of theory (DLPNO-CCSD(T) and NEVPT2) can be combined with experimental data to obtain very good rate predictions. The validity of extrapolating these predictions to higher temperatures and pressures, however, needs to be assessed in a separate study.

ASSOCIATED CONTENT

Supporting Information

The Supporting Information is available free of charge on the ACS Publications website at DOI: 10.1021/acs.jpca.9b03923.

Validation of partial error cancellation in branching ratio calculations, $R1O_2$ to Q14OOH TS figure (PDF)

ME input files, and kinetic model for the pent-1-en-3-yl + O_2 reaction system (modified Arrhenius parameters) (ZIP)

AUTHOR INFORMATION

Corresponding Author

*E-mail: arkke.eskola@helsinki.fi.

ORCID

Malte Döntgen: 0000-0002-0915-8096

Arkke J. Eskola: 0000-0002-2249-2726

Author Contributions

The investigations were conceived by A.J.E. The computational part was carried out by M.D. and T.T.P. The experiments were accomplished by T.T.P., S.P.J., R.S.T., and A.J.E. All authors contributed to writing the manuscript.

Notes

The authors declare no competing financial interest.

ACKNOWLEDGMENTS

M.D. acknowledges support from the BiofCFD project of the INNO INDIGO ERA-Net S&T Energy 2016 bio-based energy program funded by the Academy of Finland, grant number 311967. T.T.P. acknowledges support from the Doctoral Programme in Chemistry and Molecular Science of the University of Helsinki. A.J.E. and S.P.J. acknowledge support from the Academy of Finland, grant numbers 288377, 294042, and 319353. The authors wish to acknowledge CSC—IT Center for Science, Finland, for computational resources.

REFERENCES

(1) Risher, J. F.; Rhodes, S. W. *Toxicological Profile of Fuel Oils*; Agency for Toxic Substances and Disease Registry (ATSDR): Atlanta, 1995.

(2) Westbrook, C. K.; Naik, C. V.; Herbinet, O.; Pitz, W. J.; Mehl, M.; Sarathy, S. M.; Curran, H. J. Detailed chemical kinetic reaction mechanism for soy and rapeseed biodiesel fuels. *Combust. Flame* **2011**, *158*, 742−755.

(3) Sudholt, A.; Cai, L.; Heyne, J.; Haas, F. M.; Pitsch, H.; Dryer, F. L. Ignition of a bio-derived class of saturated and unsaturated furans for engine application. *Proc. Combust. Inst.* **2015**, *35*, 2957−2965.

(4) Dellinger, B.; Lomnicki, S.; Khachatryan, L.; Maskos, Z.; Hall, R. W.; Adounkpe, J.; McFerrin, C.; Truong, H. Formation and stabilization of persistent free radicals. *Proc. Combust. Inst.* **2007**, *31*, 521−528.

(5) Scheer, A. M.; Eskola, A. J.; Osborn, D. L.; Sheps, L.; Taatjes, C. A. Resonance stabilization effects on ketone autoxidation: Isomer-specific cyclic ether and ketohydroperoxide formation in the low-temperature (400 − 625 K) oxidation of diethyl ketone. *J. Phys. Chem. A* **2016**, *120*, 8625−8636.

(6) Fernandes, R. X. *Shock Tube Investigations of the Reaction Kinetics of Small Unsaturated Hydrocarbon Species*; Cuvillier Verlag: Göttingen, 2004.

(7) Lee, J.; Bozzelli, J. W. Thermochemical and kinetic analysis of the allyl radical with O_2 reaction system. *Proc. Combust. Inst.* **2005**, *30*, 1015−1022.

(8) Jenkin, M. E.; Murrells, T. P.; Shalliker, S. J.; Hayman, G. D. Kinetics and product study of the self-reactions of allyl and allyl peroxy radicals at 296 K. *J. Chem. Soc., Faraday Trans.* **1993**, *89*, 433−446.

(9) Bozzelli, J. W.; Dean, A. M. Hydrocarbon radical reactions with O_2: Comparison of allyl, formyl, and vinyl to ethyl. *J. Phys. Chem.* **1993**, *97*, 4427−4441.

(10) Georgievskii, Y.; Miller, J. A.; Klippenstein, S. J. Association rate constants for reactions between resonance-stabilized radicals:

DOI: 10.1021/acs.jpca.9b03923
J. Phys. Chem. A 2019, 123, 7897−7910

C_3H_3+C_3H_3, C_3H_3+C_3H_5, and C_3H_5+C_3H_5. *Phys. Chem. Chem. Phys.* **2007**, *9*, 4259.
(11) Hansen, N.; Miller, J. A.; Westmoreland, P. R.; Kasper, T.; Kohse-Höinghaus, K.; Wang, J.; Cool, T. A. Isomer-specific combustion chemistry in allene and propyne flames. *Combust. Flame* **2009**, *156*, 2153−2164.
(12) Rissanen, M. P.; Amedro, D.; Eskola, A. J.; Kurten, T.; Timonen, R. S. Kinetic (T = 201 − 298 K) and equilibrium (T = 320 − 420 K) measurements of the C_3H_5+O_2↔$C_3H_5O_2$ reaction. *J. Phys. Chem. A* **2012**, *116*, 3969−3978.
(13) Moradi, C. P.; Morrison, A. M.; Klippenstein, S. J.; Goldsmith, C. F.; Douberly, G. E. Propargyl + O_2 reaction in helium droplets: Entrance channel barrier or not? *J. Phys. Chem. A* **2013**, *117*, 13626−13635.
(14) Schleier, D.; Constantinidis, P.; Faßheber, N.; Fischer, I.; Friedrichs, G.; Hemberger, P.; Reusch, E.; Sztáray, B.; Voronova, K. Kinetics of the a-C_3H_5 + O_2 reaction, investigated by photoionization using synchrotron radiation. *Phys. Chem. Chem. Phys.* **2018**, *20*, 10721−10731.
(15) DeSain, J. D.; Klippenstein, S. J.; Miller, J. A.; Taatjes, C. A. Measurements, theory, and modeling of OH formation in ethyl + O_2 and propyl + O_2 reactions. *J. Phys. Chem. A* **2003**, *107*, 4415−4427.
(16) Chen, C.-J.; Bozzelli, J. W. Thermochemical property, pathway and kinetic analysis on the reactions of allylic isobutenyl radical with O_2: An elementary reaction mechanism for isobutene oxidation. *J. Phys. Chem. A* **2000**, *104*, 9715−9732.
(17) Touchard, S.; Founet, R.; Glaude, P. A.; Warth, V.; Battin-Leclerc, F.; Vanhove, G.; Ribaucour, M.; Minetti, R. Modeling of the oxidation of large alkenes at low temperatures. *Proc. Combust. Inst.* **2005**, *30*, 1073−1081.
(18) Fridlyand, A.; Goldsborough, S. S.; Brezinksy, K.; Merchant, S. S.; Green, W. H. Influence of the double bond position on the oxidation of decene isomers at high pressures and temperatures. *Proc. Combust. Inst.* **2015**, *35*, 333−340.
(19) Knyazev, V. D.; Slagle, I. R. Thermochemistry and kinetics of the reaction of 1-methylallyl radicals with molecular oxygen. *J. Phys. Chem. A* **1998**, *102*, 8932−8940.
(20) Harding, L. B.; Klippenstein, S. J.; Jasper, A. W. Ab initio methods for reactive potential surfaces. *Phys. Chem. Chem. Phys.* **2007**, *9*, 4055−4070.
(21) Eskola, A. J.; Timonen, R. S. Kinetics of the reactions of vinyl radicals with molecular oxygen and chlorine at temperatures 200-362 K. *Phys. Chem. Chem. Phys.* **2003**, *5*, 2557−2561.
(22) Yaws, C. L. *Yaw's Handbook of Antoine Coefficients for Vapor Pressure*, 2nd ed.; Knovel: New York, 2005.
(23) Dean, J. A. *Lange's Handbook of Chemistry*; McGraw-Hill, Inc.: New York, 1998.
(24) Curtiss, L. A.; Redfern, P. C.; Raghavachari, K. Gaussian-4 theory. *J. Chem. Phys.* **2007**, *126*, 084108.
(25) Yu, H. S.; He, X.; Li, S. L.; Truhlar, D. G. MN15: A Kohn-Sham global-hybrid exchange-correlation density functional with broad accuracy for multi-reference and single-reference systems and noncovalent interactions. *Chem. Sci.* **2016**, *7*, 5032−5051.
(26) Frisch, M. J.; Trucks, G. W.; Schlegel, H. B.; Scuseria, G. E.; Robb, M. A.; Cheeseman, J. R.; Scalmani, G.; Barone, V.; Petersson, G. A.; Nakatsuji, H.; et al. *Gaussian 16* Revision B.01. 2016; Gaussian Inc.: Wallingford CT, 2016.
(27) Van Veen, G. N. A.; Baller, T.; De Vries, A. E. Photofragmentation of CH_3Br in the A band. *Chem. Phys.* **1985**, *92*, 59−65.
(28) Escure, C.; Leininger, T.; Lepetit, B. Ab initio study of methylbromide photodissociation in the Ã band. *J. Chem. Phys.* **2009**, *130*, 244305.
(29) Neese, F. The ORCA program system. *Wiley Interdiscip. Rev.: Comput. Mol. Sci.* **2012**, *2*, 73−78.
(30) Grimme, S.; Neese, F. Double-hybrid density functional theory for excited electronic states of molecules. *J. Chem. Phys.* **2007**, *127*, 154116.
(31) Underwood, J. G.; Powis, I. Photofragmentation of CH_3Br in the red wing of the first continuum absorption band. *Phys. Chem. Chem. Phys.* **2000**, *2*, 747−756.
(32) Kokh, D. B.; Liebermann, H.-P.; Buenker, R. J. Photodissociation of CH_3Cl, C_2H_5Cl, and C_6H_5Cl on the Ag(111) surface: Ab initio embedded cluster and configuration interaction study. *J. Chem. Phys.* **2010**, *132*, 074707.
(33) Grimme, S. Semiempirical hybrid density functional with perturbative second-order correlation. *J. Chem. Phys.* **2006**, *124*, 034108.
(34) Grimme, S.; Ehrlich, S.; Goerigk, L. Effect of the damping function in dispersion corrected density functional theory. *J. Comput. Chem.* **2011**, *32*, 1456−1465.
(35) Riplinger, C.; Pinski, P.; Becker, U.; Valeev, E. F.; Neese, F. Spare maps − a systematic infrastructure for reduced-scaling electronic structure methods. II. Linear scaling domain based pair natural orbital coupled cluster theory. *J. Chem. Phys.* **2016**, *144*, 024109.
(36) Saitow, M.; Becker, U.; Riplinger, C.; Valeev, E. F.; Neese, F. A new near-linear scaling, efficient and accurate, open-shell domain-based local pair natural orbital coupled cluster singles and doubles theory. *J. Chem. Phys.* **2017**, *146*, 164105.
(37) Halkier, A.; Helgakerb, T.; Jørgensena, P.; Klopperb, W.; Kocha, H.; Olsenc, J.; Wilsond, A. K. Basis-set convergence in correlated calculations on Ne, N_2, and H_2O. *Chem. Phys. Lett.* **1998**, *286*, 243−252.
(38) Angeli, C.; Cimiraglia, R.; Evangelisti, S.; Leininger, T.; Malrieu, J.-P. Introduction of n-electron valence states for multi-reference perturbation theory. *J. Chem. Phys.* **2001**, *114*, 10252.
(39) Goldsmith, C. F.; Harding, L. B.; Georgievskii, Y.; Miller, J. A.; Klippenstein, S. J. Temperature and pressure-dependent rate coefficients of the reaction of vinyl radical with molecular oxygen. *J. Phys. Chem. A* **2015**, *119*, 7766−7779.
(40) Schapiro, I.; Sivalingam, K.; Neese, F. Assessment of n-electron valence state perturbation theory for vertical excitation energies. *J. Chem. Theory. Comput.* **2013**, *9*, 3567−3580.
(41) Zobel, J. P.; Nogueira, J. J.; González, L. The IPEA dilemma in CASPT2. *Chem. Sci.* **2017**, *8*, 1482−1499.
(42) Pechukas, P.; Light, J. C. On detailed balancing and statistical theories of chemical kinetics. *J. Chem. Phys.* **1965**, *42*, 3281.
(43) Georgievskii, Y.; Miller, J. A.; Burke, M. P.; Klippenstein, S. J. Reformulation and solution of the master equation for multi-well chemical reactions. *J. Phys. Chem. A* **2013**, *117*, 12146−12154.
(44) Gao, C. W.; Allen, J. W.; Green, W. H.; West, R. H. Reaction mechanism generator: Automatic construction of chemical kinetic mechanisms. *Comput. Phys. Commun.* **2016**, *203*, 212−225.
(45) Poling, B. E.; Prausnitz, J. M.; O'Connell, J. P. *The Properties of Gases and Liquids*; McGraw-Hill: New York, 2000.
(46) Hippler, H.; Troe, J.; Wendelken, H. J. Collisional deactivation of vibrationally highly excited polyatomic molecules. II. Direct observations of excited toluene. *J. Chem. Phys.* **1983**, *78*, 6709−6717.
(47) Atkinson, D. B.; Hudgens, J. W. Rate coefficients for the propargyl radical self-reaction and oxygen addition reaction measured using ultraviolet cavity ring-down spectroscopy. *J. Phys. Chem. A* **1999**, *103*, 4242−4252.
(48) Timberlake, J. W.; Hodges, M. L. Substituent effects and free radical stability. The methoxy group. *Tetrahedron Lett.* **1970**, *11*, 4147−4150.
(49) Tsang, W. Chemical kinetic data base for combustion chemistry. Part V. Propene. *J. Phys. Chem. Ref. Data* **1991**, *20*, 221−273.
(50) Blanksby, S. J.; Ellison, G. B. Bond dissociation energies of organic molecules. *Acc. Chem. Res.* **2003**, *36*, 255−263.
(51) Paulechka, E.; Kazakov, A. Efficient DLPNO-CCDS(T)-based estimation of formation enthalpies for C-, H, O-, and N-containing closed-shell compounds validated against critically evaluated experimental data. *J. Phys. Chem. A* **2017**, *121*, 4379−4387.
(52) Eskola, A. J.; Carr, S. A.; Shannon, R.; Wang, B.-S.; Blitz, M. A.; Pilling, M. J.; Seakins, P.; Robertson, S. H. Analysis of the kinetics and

DOI: 10.1021/acs.jpca.9b03923
J. Phys. Chem. A 2019, 123, 7897−7910

yields of OH radical from the $CH_3OCH_2+O_2$ reaction in the temperature range 195 − 600 K: An experimental and computational study. *J. Phys. Chem. A* **2014**, *118*, 6773−6788.
(53) Fernandes, R. X.; Luther, K.; Troe, J. Falloff curves for the reaction $CH_3+O_2(+M)\rightarrow CH_3O_2(+M)$ in the pressure range 2-1000 bar and the temperature range 300-700 K. *J. Phys. Chem. A* **2006**, *110*, 4442−4449.
(54) Döntgen, M.; Leonhard, K. Discussion of the separation of chemical and relaxational kinetics of chemically activated intermediates in master equation simulations. *J. Phys. Chem. A* **2017**, *121*, 1563−1570.
(55) Goodwin, D. G.; Moffat, H. K.; Speth, R. L. *Cantera: An Object-Oriented Software Toolkit for Chemical Kinetics, Thermodynamics, and Transport Processes*, version 2.2.1, 2016, http://www.cantera.org.
(56) Zhong, B.-J.; Peng, H.-S. Measurement of laminar flame speed and chemical kinetic model of 1-pentene/air mixtures. *Combust. Sci. Technol.* **2017**, *189*, 1698−1712.
(57) Matheu, D. M.; Green, W. H.; Grenda, J. M. Capturing pressure-dependence in automated mechanism generation: Reactions through cycloalkyl intermediates. *Int. J. Chem. Kinet.* **2003**, *35*, 95−119.
(58) Zhou, C.-W.; Li, Y.; O'Connor, E.; Somers, K. P.; Thion, S.; Keesee, C.; Mathieu, O.; Petersen, E. L.; DeVerter, T. A.; Oehlschlaeger, M. A.; et al. A comprehensive experimental and modeling study of isobutene oxidation. *Combust. Flame* **2016**, *167*, 353−379.
(59) Goldsmith, C. F.; Green, W. H.; Klippenstein, S. J. Role of O_2+QOOH in low-temperature ignition of propane. 1. Temperature and pressure dependent rate coefficients. *J. Phys. Chem. A* **2012**, *116*, 3325−3346.

DOI: 10.1021/acs.jpca.9b03923
J. Phys. Chem. A 2019, 123, 7897−7910